# Chapter Five: Molecular Camouflage by a Context-Specific Hydrogel as the Key to Unlock the Potential of Viral Vector Gene Therapy

## 5.1 Preamble

Having prepared and characterized different libraries of Fmoc-SAP hydrogel materials as delivery vehicles, the next step was the investigation of a tissue-specific molecular hydrogel to package recombinant adeno-associated viruses (rAAVs). After confirming the delivery pathway, a set of rAAV variants were assessed for their ability to transduce various types of rodent and human neural cells *in vitro* and *in vivo*.

This chapter describes work done on a project to demonstrate that the protective environment provided by advanced biomaterials can function as injectable gene carriers to focus their therapeutic potential.

The materials and experimental methodology used in this chapter were described in Chapter 3.

**Publication relevant to this chapter:**

**Shiva Soltani Dehnavi**, Arianna Cembran, Negar Mahmoudi, Lilith M Caballero Aguilar, Yi Wang, Samuel Cheeseman, Nicolo Malagutti, Stephanie Franks, Benjamin Long, Leszek Lisowski, Alan R Harvey, Clare L. Parish, Richard J. Williams, David R. Nisbet, Molecular camouflage by a Context-Specific hydrogel as the key to unlock the potential of viral vector

gene therapy. Chemical Engineering Journal, 477 (2023) 146857, (https://doi.org/10.1016/j.cej.2023.146857).



*Please see Appendix D for access to this publication*.

Some parts of this paper were also included in the Master of Philosophy thesis entitled "Hydrogels-based viral vectors delivery: a self-assembly strategy for targeted gene therapy", conducted by Arianna Cembran.

## 5.2 Abstract

Gene therapy offers hope for currently untreatable diseases; the patient's own cellular machinery is recruited to create therapeutics. However, unpredictable responses that lead to neutralization by the host immune system and issues in constraining, controlling, and sustaining delivery have presented clinical barriers to otherwise promising therapeutic developments. Here, we show that the protective environment provided by advanced biomaterials can function as injectable gene carriers to focus their therapeutic potential. Firstly, we investigated the potential of a tissue-specific molecular hydrogel to package recombinant adeno-associated viruses (rAAVs). Once a delivery pathway was confirmed, a set of rAAV variants were subsequently assessed for their ability to transduce various types of rodent and human neural cells in vitro and in vivo. Based on GFP expression, we identified a relatively new variant, rAAV-DJ, as showing desirable characteristics for constrained delivery and transduction efficiency. For the first time, we demonstrated precise control over the strength and type of interaction between biomaterials and rAAVs enabling the programmed release of

viral payloads. This new approach enables specific infection of desired anatomical targets in a programmed fashion.

### *5.2.1 Graphical Abstract*

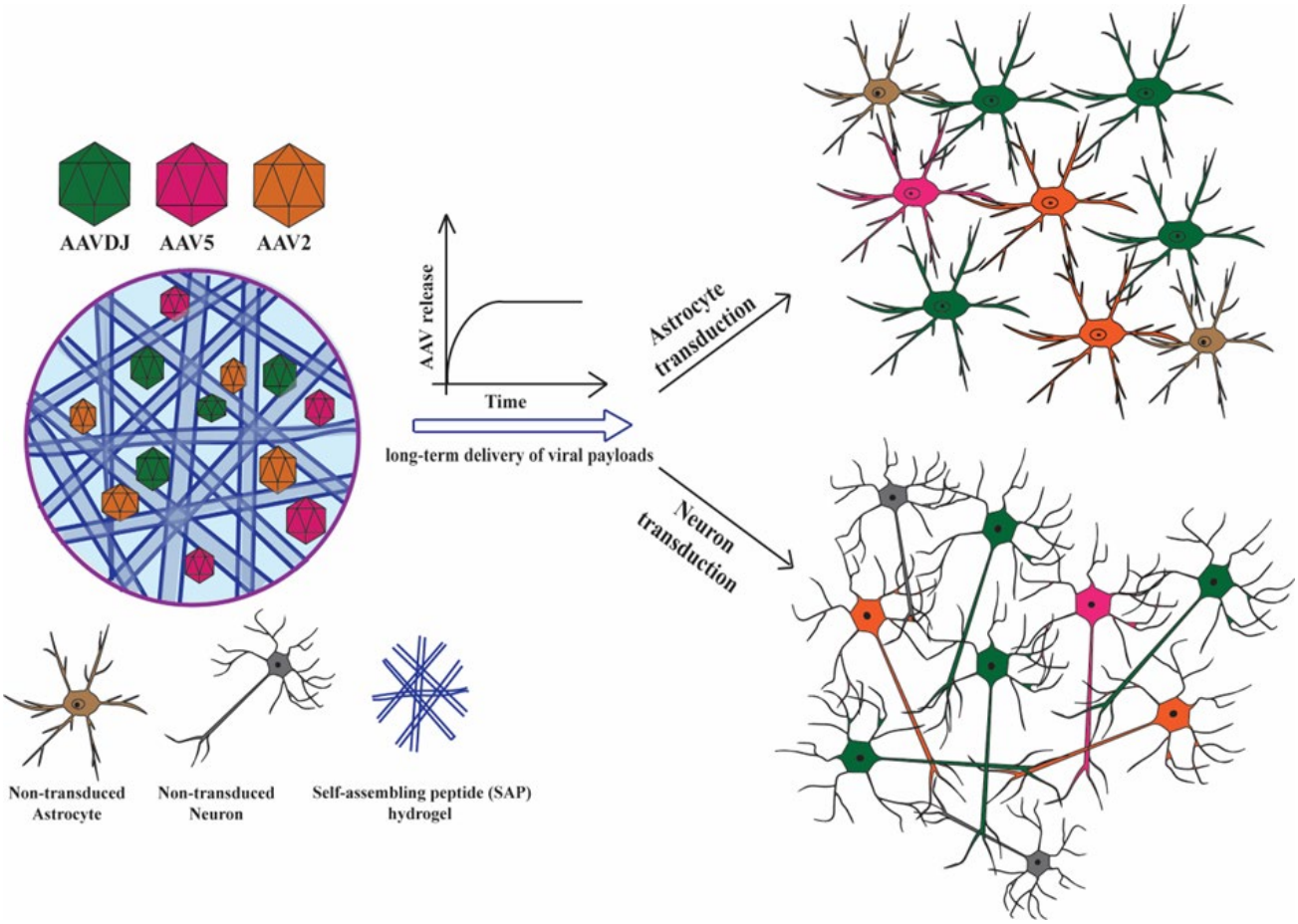

## 5.3 Introduction

Due to its ability to replace, silence or substitute defective genes, gene therapy has become a promising approach to tackle many prominent and widespread health conditions, including haemophilia [293-295], cancers [296], traumatic brain injuries [297], and neurodegenerative disorders [298, 299]. This optimism is generated because of gene therapy's potential as an excellent method for delivering therapeutic agents directly to damaged or disease tissues and cells *in vivo* and e*x vivo* [5, 96]. To realise this, a technological advance is now needed for successful clinical translation; mechanisms should be developed to make gene therapy both predictable and targeted. The two key parameters that must be addressed are: i) accurate insertion and activation of the corrective genes without causing adverse effects, and ii) effective, targeted delivery of the genetic material to relevant cells in compromised tissues.

There have been many efforts to address the first goal, with various techniques available to incorporate new genetic material into a host. In recent years, researchers have developed a DNAzyme-based gene delivery system that is responsive to microRNAs (miRNA) or mRNA to achieve targeted delivery [300]. MiRNAs are short, untranslated, regulatory RNA molecules that lead to the degradation of target mRNAs or the suppression of mRNA translation, thereby inhibiting the synthesis of proteins and achieving the regulation of genes [301, 302]. To provide a tightly controlled gene expression of miRNAs, they are being combined with other targeting strategies such as capsid-modified viral vectors or surface-modified non-viral vectors. Viral vectors are regarded as the preferred option due to their ability to deliver therapeutic cargo to specific target cells with diagnostically measurable, persistent effects. Specifically, vectors based on adeno-associated viruses (AAVs) have gained particular attention over other vector systems because they are easily modified and versatile, and have advantages due to their non-pathogenicity, lower cytotoxicity, ability to transduce both dividing and non-dividing cells, variable tropism (several serotypes) and– dependent on the promoter [1, 303]– high persistence

of transgene expression in non-dividing cells [94, 304]. All of these characteristics make recombinant AAVs (rAAVs) excellent candidates for clinical purposes, including applications in the central nervous system (CNS) [305]. However, despite hundreds of clinical trials to date and a number of AAV-based therapies reaching market approval, it is clear that further research is required to address various technical challenges that have restricted the broader application of AAV-based gene therapeutics in the clinic, including, ongoing identification of appropriate AAV serotypes for specific tissues, and a practicable pathway to the individual cell types within said tissues[306, 307]. As such, here we report a powerful and synergistic marrying up of new AAVs with rationally designed delivery tools.

This informs our second goal, the targeted transduction of desired anatomical targets in a clinically compatible fashion. To improve efficacy, we must develop methods to enable controlled and sustained delivery of a viral vector, while avoiding humoral immune responses that often neutralize the vector. This was our motivation to engineer an advanced, programmable AAV delivery system to improve efficacy, specificity and, through the incorporation of molecular signals to ensure protection of the vector from viral clearance by the immune system [218].

The use of hydrogels for gene delivery using viral vectors has attracted attention in recent years, due to their capacity for encapsulating and/or immobilising viral vector payloads while simultaneously providing protection against immune clearance [134, 308-310]. Moreover, viral vector encapsulation into spatially confining hydrogels has the potential to minimise the delivery of genetic payload to off-target cells and/or organs, while simultaneously encouraging their controlled release into preferred targets. Beyond viral vector delivery, engineered hydrogels and other biomaterials have contributed to improved outcomes for many applications including reproductive medicine [311], anti-infective therapies [312], wound healing [313], and dental tissue regeneration [314], amongst other applications [315]. Fibre-based delivery

strategies have also been demonstrated as controllable and programmable drug delivery systems [316]. Thus far, alginate [317], fibrin [155, 318] and self-assembled peptides (SAPs) [160, 278] have exhibited successful encapsulation and release of both rAAV and lentiviral vectors (LV). Yet, depending on the population of cells that need to be targeted within a given tissue, it remains a challenge to engineer a delivery system that is able to program the delivery of multiple serotypes without disrupting the benign environment of the material. In nature, surface structures on the AAV interact in a noncovalent fashion with membrane receptors on the surface of the cell. This process allows the virus to bind and deliver its payload specifically to a target cell [319]. Here, we present a molecular hydrogel that exploits this innate binding force, demonstrating its efficacy as a programmable delivery system.

SAPs are a specific class of molecular biomaterials that spontaneously assemble *in situ* to form a stable macroscale hydrogel with a hierarchical structure that is present on a scale similar to the distribution of extracellular matrix (ECM) proteins. They are known for their controllable "bottom-up" fabrication and their capacity to self-assemble via non-covalent interactions into what is typically a decorated 1D nanofibrous network [24, 320]. Through careful sequence design, these nanofibrous networks have proven to be effective chemical and morphological mimics of the extracellular matrix (ECM), and therefore are able to concomitantly provide mechanical, chemical and biological cues to support cells [20]. Additionally, SAPs allow for the incorporation of biologically relevant epitopes to achieve ideal biocompatibility and functionality [24]. For example, SAP hydrogels with a laminin-derived IKVAV epitope, have been shown to be beneficial to neuron cells and astrocyte cells [227, 321, 322]. This flexibility of control over the parameters that define their function and assembly means that SAPs can be easily engineered for specific tissue applications, making them one of the most promising biomaterials for a wide range of biomedical applications, including CNS repair and reconstruction [323]. Recently, we have made substantial progress in showing how these

systems can be readily adapted to several applications including cell culture *in vitro* [324], cell transplantation [225, 325], and incorporation and delivery of growth factors [13, 22] and drugs [326, 327].

Almost all studies to date have focussed on rAAV transduction of neurones and, as such, comparatively little is known about astrocytic tropism in different parts of the CNS [328]. This is an important consideration as the therapeutic modification of astrocytes may be useful after neurological injury. For instance, post-insult astrocytes become activated, proliferating and migrating to phagocytose foreign materials, damaged proteins, etc., before returning to a homeostatic state [326]. Therefore, the genetic modification of activated astrocytes has the potential to provide a new source of neurones and other cell types, to repair and possibly reinnervate damaged CNS tissue [329, 330].

The aim of this study was therefore to investigate the ability of our specifically designed SAPs to encapsulate and release a small mix of different rAAV variants known to be specific to glia and neurones (rAAV2, rAAV5) and a novel variant for assessment (rAAV-DJ). It is known that rAAV serotypes bind differently to cell-surface receptors based on their unique surface structures [304]. We hypothesized that the surface properties of the 1D benign peptide hydrogel would not only enable these vectors to maintain their activity throughout their encapsulation and release but that the different steric hindrance and reversible electrostatic affinities between the viral vector capsids and the nanofibrillar mesh would tune the release profile. To this end, we tested the three rAAV variants for their ability to transduce rodent primary cortical neurons and astrocytes, as well as human astrocytes (visualized through green fluorescent protein (GFP) expression). We found that the rAAV-DJ variant presented high transduction rates in all three cell types, while rAAV2 favoured neurons and rAAV5 exhibited the lowest cell transduction efficiency across all three cell types. The viral vector release profiles were compared for four different formulations of SAPs, with varying structures and charges. The rAAV variants

showed different release profiles based on the distinct combination of biomaterials and vectors. Our results indicate that SAP systems are capable of sustained release of several rAAV particles, with material-specific delivery profiles. Therefore, depending on the application and release requirement, SAPs can be engineered to program the release of AAVs and their delivery to the target by an optimal pairing of the molecular hydrogel and AAV variant [225, 227, 331]. Moreover, to our knowledge, we provide the first report that one of the bioengineered rAAV variants (AAV-DJ) can effectively transduce astrocytes *in vitro*.

## 5.4 Results

### *5.4.1 Effective Cell Transduction of rAAV-DJ In Vitro*

**Among the three rAAV variants, rAAV-DJ shows high tropism for both neurons and astrocytes *in vitro*.**

Firstly, we evaluated the rAAV serotype that can most effectively transduce cortical neurons and/or astrocytes when delivered from our material. We prepared a small mix consisting of rAAV2, rAAV5, and rAAV-DJ for assessment, with encoded eGFP as a reporter. In the first set of experiments, we tested the rAAV transduction rates on three distinct cell types: primary murine cortical neurons, primary murine astrocytes, and a human astrocyte cell line (ScienCell Research Laboratories, CA, USA) (**Figure 5.1**). All experiments were performed using the same vector per cell dose (MOT = $10^5$ vg/cell) and the readout was performed at 72 hrs. All rAAVs tested could effectively transduce neurons and astrocytes, as confirmed by strong GFP expression (**Figure 5.1**). Interestingly, significantly different levels of transduction were observed between the viral vectors tested, with rAAV-DJ consistently presenting the highest tropism across all cell types (**Figure 5.1 (panels G, H, and I)).** As expected, rAAV2 demonstrated more efficient transduction of neurons (37%) (**Figure 5.1-J**)) than the mouse (6%) (**Figure 5.1-k))** and human astrocytes (28%) (**Figure 5.1-L**), which is consistent with previously published literature [332, 333]. Interestingly, rAAV5 demonstrated lower levels of transduction compared to rAAV2 and showed the lowest levels of cell transduction across all three cell types. Flow cytometry was also performed to understand the percentage of GFP+ βIII-Tubulin+ cells (**Figure 5.2-A**) for each of the viral vector systems as well as GFP+ GFAP+ cells within primary (**Figure 5.2-B**) and human astrocytes (**Figure 5.2-C**).

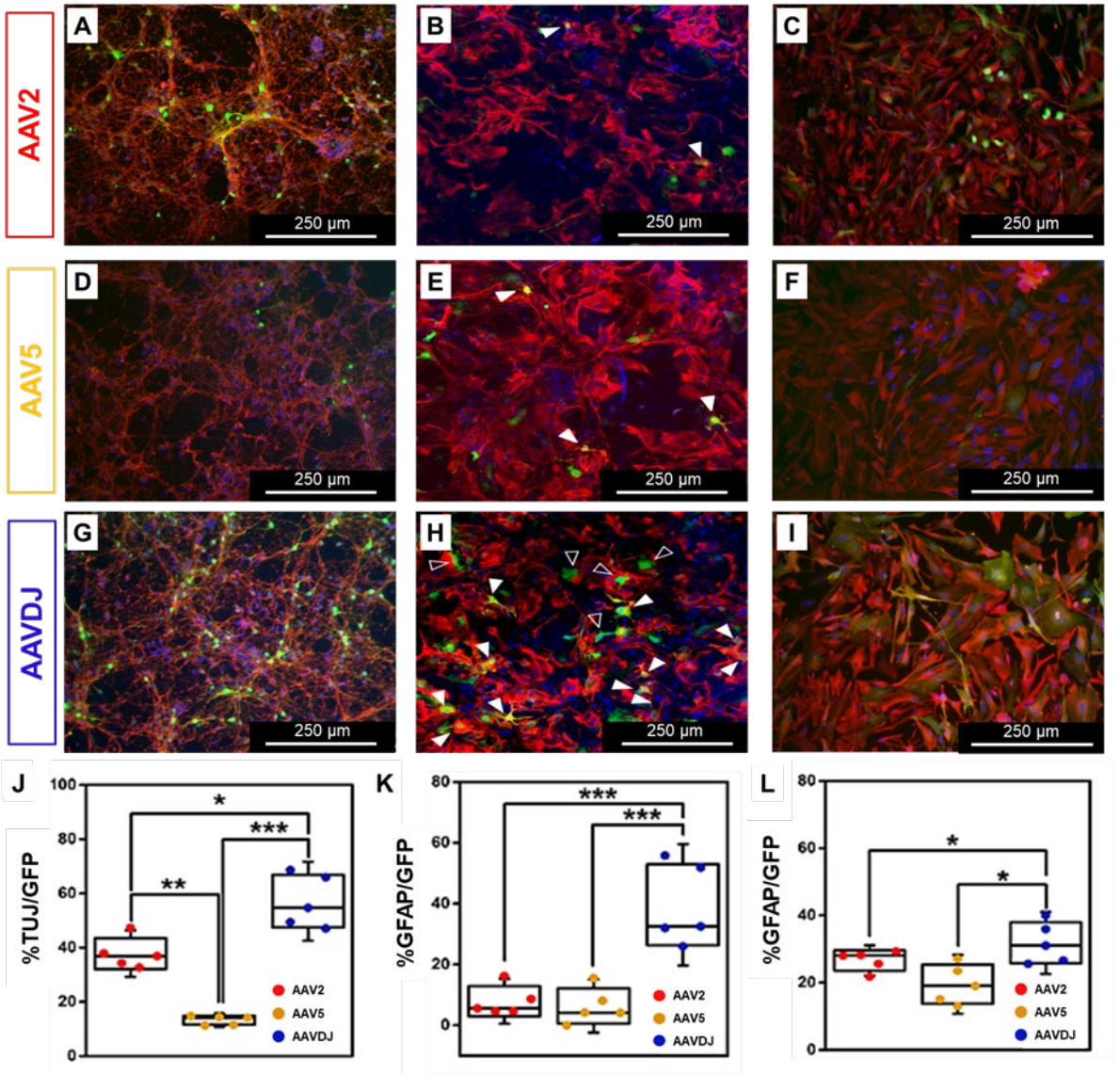


***Figure 5-1 Transduction of primary cortical neurons, primary astrocytes, and human astrocytes with three rAAV-GFP vectors.*** *All cells were transduced with 105 vg/cell of either rAAV2, rAAV5 and rAAV-DJ for 72 h. Cultures were immunostained with GFP (**green**) to visualize the GFP virally transduced cells and counterstained with DAPI (to visualise all cells). In addition, primary cortical neurons (**A, D and G**) were stained for the neural marker βIII-Tubulin (**red**) whilst astrocytic cells (mouse, **B, E and H**, and human, **C, F and I**) were stained for the astrocytic marker GFAP (**red**). Arrowheads indicate harder to see colocalization signals (**B, E and H**). Quantification of transduced cell types is represented in percentage of cells positive for GFP and specific markers (**J, K and L**). Data represents mean ± SD. ANOVA with Tukey's post-hoc statistical testing to compare statistical differences between groups where *p < 0.05; ** p < 0.01; *** p < 0.001.*

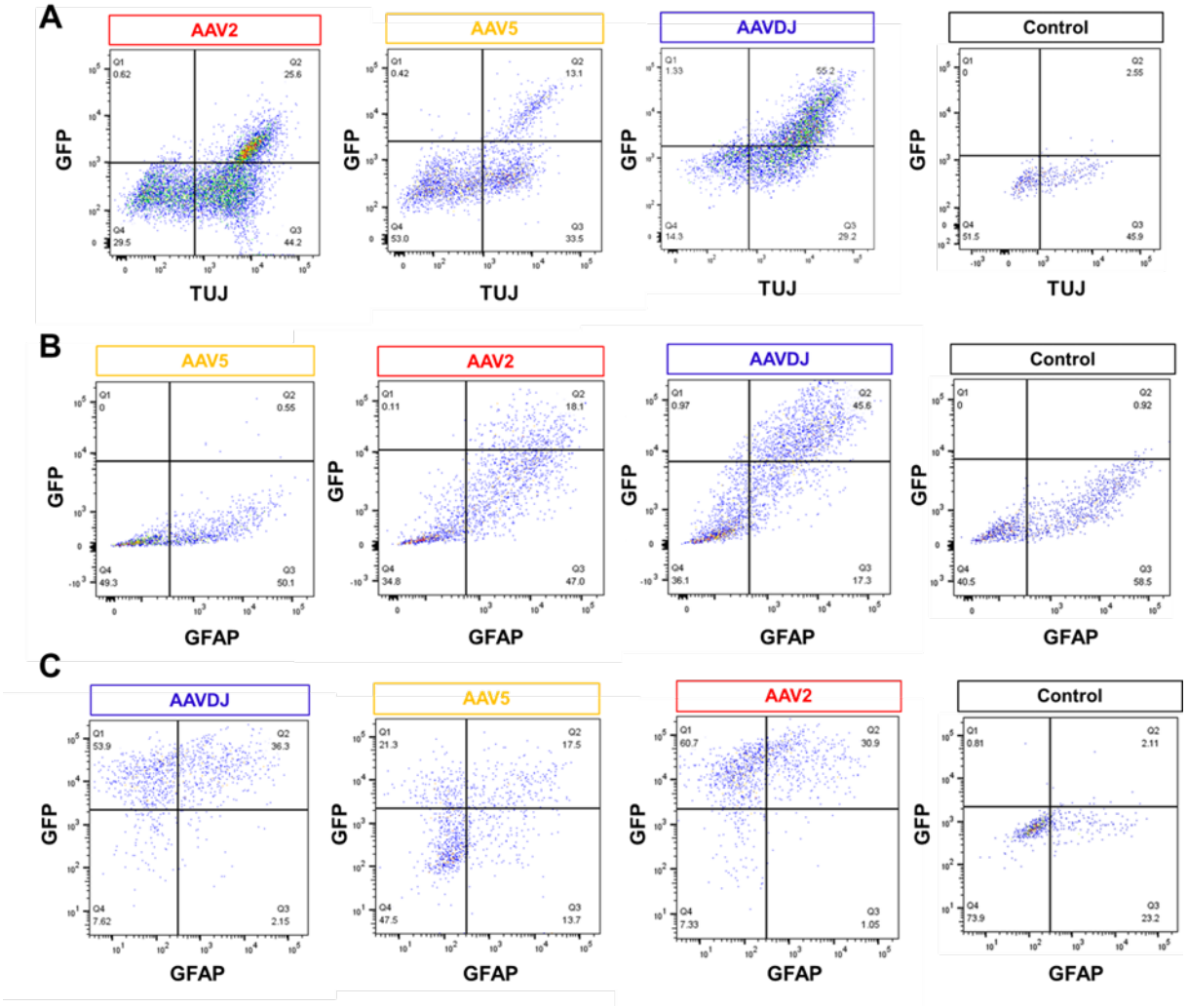


***Figure 5-2 Flow Cytometry analysis results.*** ***(A)*** *shows the total percentages of GFP+ βIII-Tubulin+ cells for three different viral vector systems (rAAV-DJ, rAAV2, and rAAV5).* ***(B)*** *and* ***(C)*** *show the total percentages of GFP+ GFAP+ cells (primary astrocytes and human astrocytes, respectively) for three different viral vector systems (rAAV-DJ, rAAV2, and rAAV5).*

### *5.4.2 Effective Cell Transduction of rAAV-DJ In Vivo*

Next, we tested if efficient transduction of rAAV-DJ also occurred in vivo. rAAV-DJ injection led to a significant increase in neuron transduction compared to rAAV2 and rAAV5 (**Figure 5.3**). Surprisingly, after these cortical injections rAAV2 also showed moderate levels of astrocytic transduction compared to neuronal transduction (**Figure 5.3 (A and D)**). Ultimately,

each vector was able to efficiently transduce cortical brain tissue, and after 12 days GFP expression was evenly dispersed and consistent.

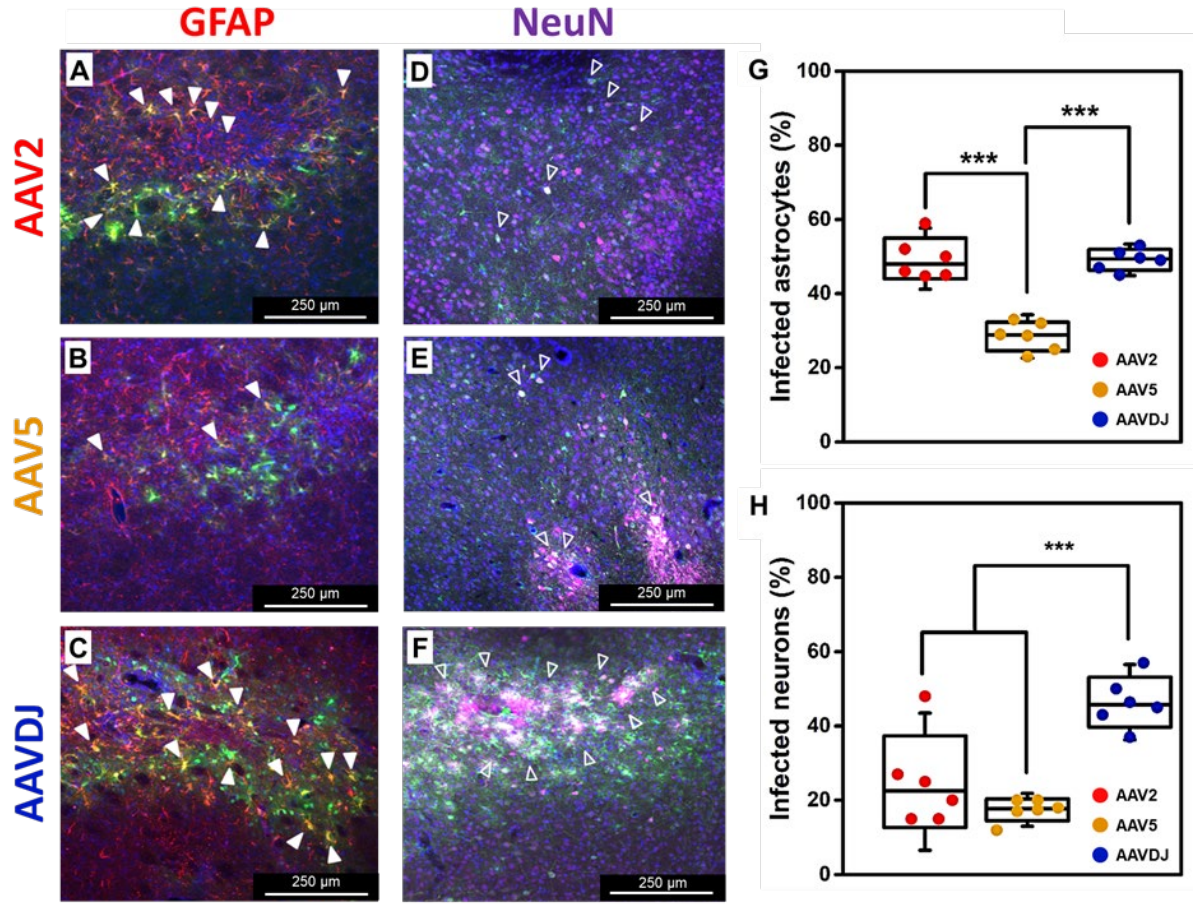


***Figure 5-3 Transduction by rAAV2, rAAV5 and rAAV-DJ in mouse cortex.*** *Representative images at the rAAV injection sites illustrating GFP transduced cells* ***(green)*** *co-labelled with astrocytic marker GFAP (red, A-C) or neuronal marker NeuN* ***(magenta, D-F)*** *for the 3 rAAV variants – AAV2* ***(A and D),*** *AAV5* ***(B and E)*** *and AAVDJ* ***(C and F).*** *Arrowheads indicate colocalization cells. Results represent the percentage of transduced astrocytes and neurons analysed by ANOVA with Tukey's post-hoc statistical testing to compare statistical differences between groups *** $p < 0.001$.*

### *5.4.3 Material Characterization of Fmoc-SAP Systems*

These data reveal that all three AAV variants were able to efficiently transduce cortical cells, with rAAV-DJ labelling the greatest proportion of cells when applied either *in vitro* or *in vivo*. However, we wished to extend this study further and attempt to address issues associated with controlling, targeting and sustaining delivery. Ultimately, we wanted to determine if these biomaterials could be optimised to improve the efficiency, distribution, and kinetics of the delivered vectors from a material that supported and matched the surrounding tissue. Therefore, to support the integration of the viral vectors, we fabricated several Fmoc-SAP hydrogel scaffolds with biomimetic properties of the brain's native ECM. All of the synthesised scaffolds included the laminin domain epitope sequence IKVAV, which is necessary for important neural processes such as differentiation, adhesion, migration and axonal plasticity. In these SAPs, the presence of the aromatic Fmoc moiety drives π-β self-assembly, while the bioactive peptide sequence contributes to the scaffold's ability to direct cell behaviour and provide structural support through its nanofibrous matrix. We hypothesised that these scaffolds would be able to non-specifically incorporate viral vectors via non-covalent, reversible interactions between vector payloads and the SAP systems by taking advantage of the ease of their fabrication. We used the previously designed Fmoc-DDIKVAV and further developed this to design a library of three additional Fmoc-SAP systems (**Figure 5.4-A**): Fmoc-DDIKVAVK, already functionalised via an increased positive charge with additional -NH2 groups at the C-terminus; Fmoc-DIKVAVD for its negative -COOH groups at the C-terminus; and Fmoc-DDIKVAVL for the hydrophobic contribution of side chain isobutyl groups at its C-terminus (**Figure 5.4-A)**. We also hypothesized that a co-assembly of Fmoc-DDIKVAVK and Fmoc-DIKVAVD could result in a distribution of the positive and negative charges in electrostatically stable structures. The gelation of all SAP systems is pH-driven (**Figure 5.5)**. The existence of positively charged amine (NH2+) moieties would increase the electrostatic

attraction with the negatively charged membranes on the protein shell of a virus and cell surface, which boosts the virus's capability to attach to the cell membrane and, subsequently, deliver its genetic cargo.

The formation of the nanofibrous structure was confirmed by TEM (**Figure 5.4, panels B-E)**). The Fmoc-SAP systems all showed a consistent nanofibrous network, confirming that the nanofibrous assembly was preserved. TEM micrographs displayed a more branched, intertwined architecture for the co-assembled system and Fmoc-DDIKVAVL, potentially due to the increased hydrophobicity and relative charges at the C terminus, respectively (**Figure 5.4**, **panels D, E** and **Figure 5.6**), resulting in a broader distribution of diameter. Conversely, Fmoc-DDIKVAVK and Fmoc-DIKVAVD formed fibres with more uniform diameters, possibly due to differential packing within the structures due to the N terminal residue (**Figure 5.4, panels B, C** and **Figure 5.6)**.

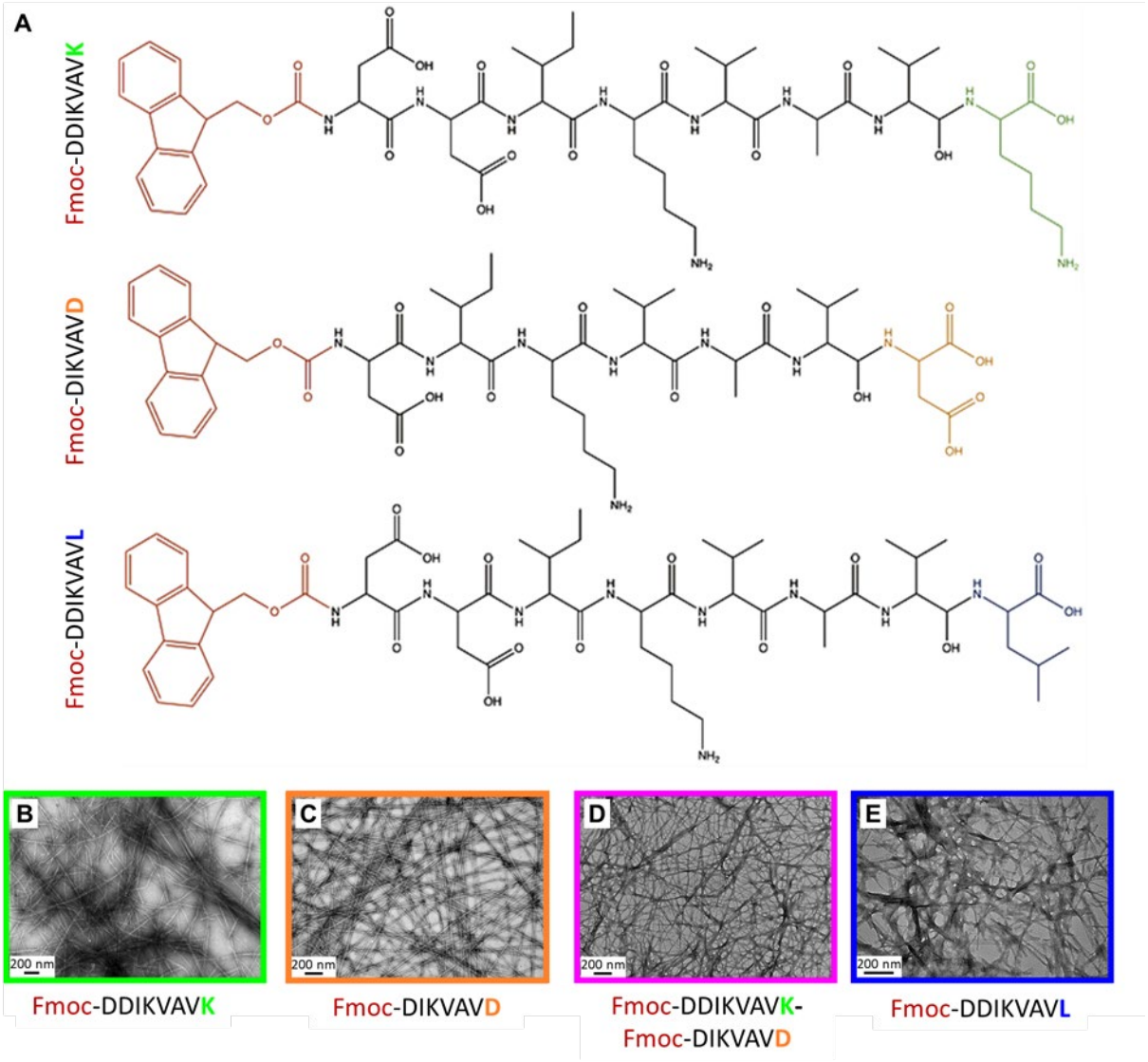


***Figure 5-4*** *Chemical structure of Fmoc-SAP systems* ***(A).*** *TEM images of Fmoc-SAP systems* ***(B-E).*** *TEM images demonstrate the nanofiber structures of single SAP systems* ***(B)*** *Fmoc-DDIKVAVK,* ***(C)*** *Fmoc-DIKVAVD,* ***(D)*** *the co-assembled Fmoc-DDIKVAVK-DIKVAVD and* ***(E)*** *Fmoc-DDIKVAVL. Scale bars are all 200 nm.*

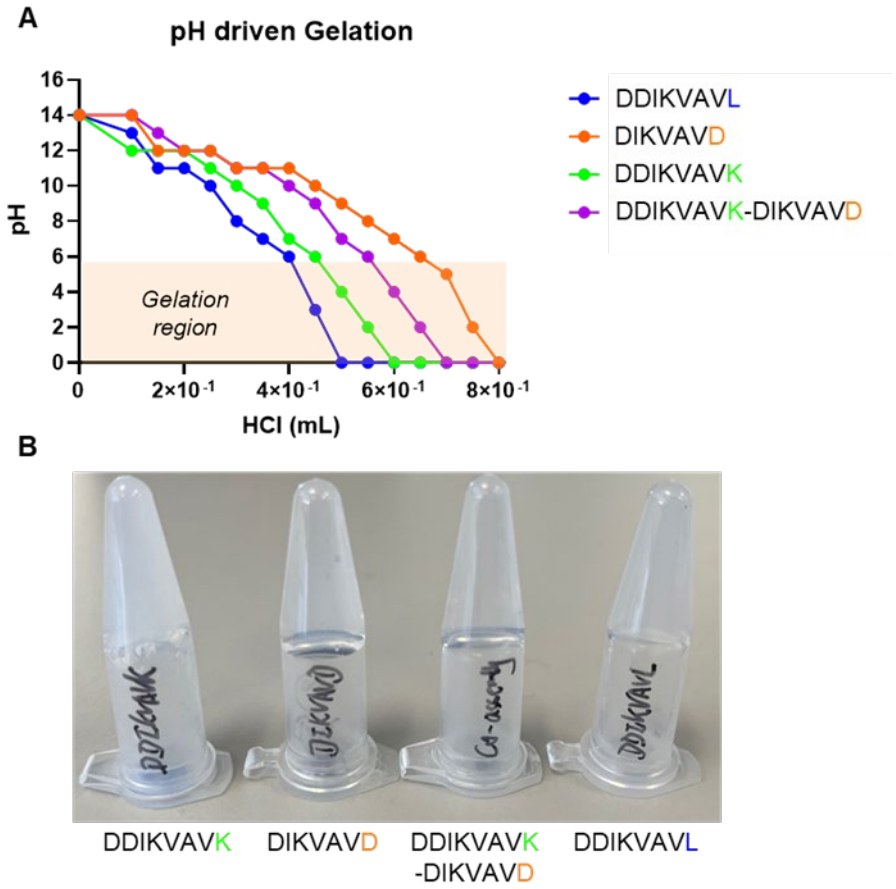


***Figure 5-5 (A)*** *pH-driven gel formation of the SAPs.* ***(B)*** *Photographs of SAP hydrogels that have undergone gelation.*

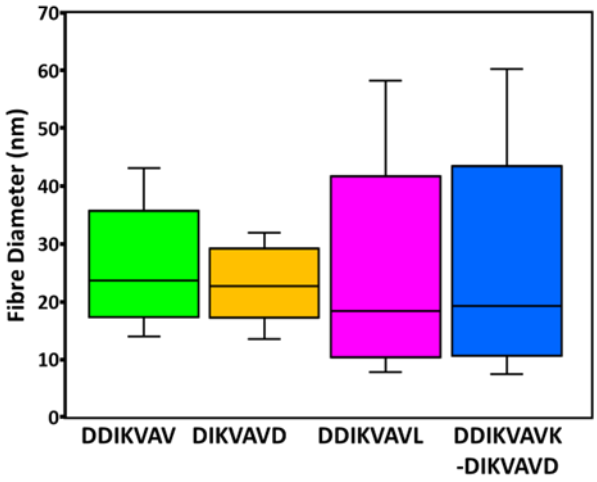


***Figure 5-6 Fibre diameter of the different peptides.*** *Measurements taken from TEM images (n=50) using FIJI (ImageJ) image processing software.*

Mass spectrometry analysis of the DDIKVAVK, DIKVAVD and DDIKVAVL peptides demonstrated an abundance of a single component (**Figure 5.7**), while high-performance liquid chromatography (HPLC) revealed a single peak (**Figure 5.8**), representative of pure samples.

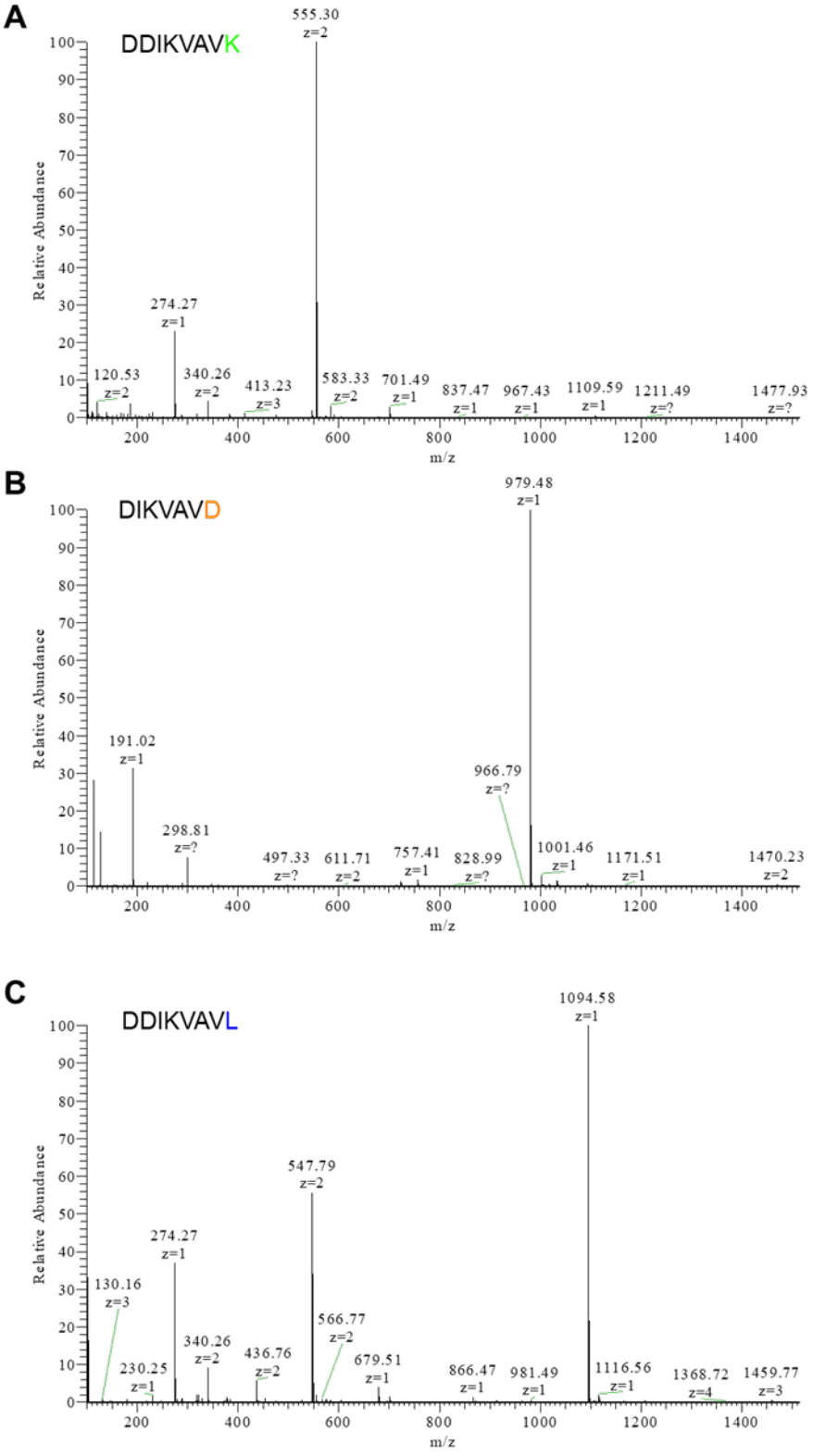


***Figure 5-7 Mass spectrometry*** *analysis of* ***(A)*** *DDIKVAVK,* ***(B)*** *DIKVAVD and* ***(C)*** *DDIKVAVL. The data demonstrates an abundance of a single component, with some small degradation products.*

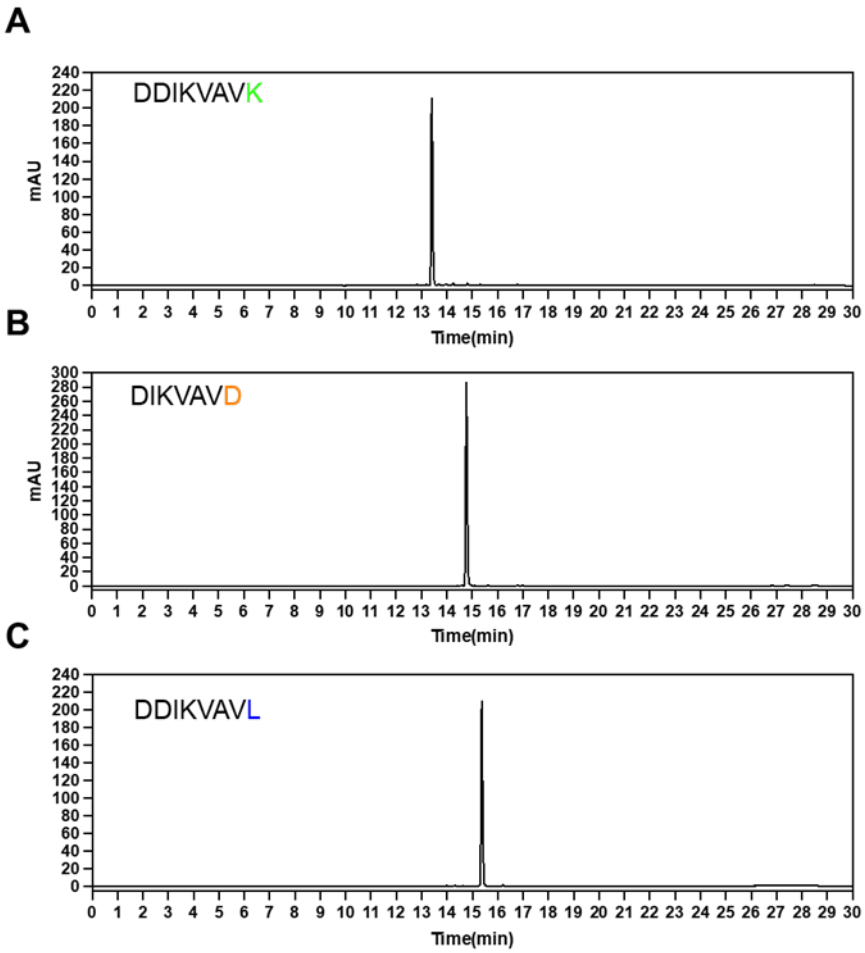


***Figure 5-8 High-performance liquid chromatography (HPLC)*** *analysis of* ***(A)*** *DDIKVAVK,* ***(B)*** *DIKVAVD and* ***(C)*** *DDIKVAVL. The data demonstrates a single peak, representative of pure samples.*

SAXS data analysis results were found to reinforce the observations made by TEM images regarding the morphology of gels Fmoc-DIKVAVD, Fmoc-DDIKVAVL and Fmoc-DDIKVAVK/Fmoc-DIKVAVD (**Figure 5.9 (A-B))**. Log-log plots of scatter intensity I(q), shown in (**Figure 5.9-A**), revealed an inverse proportionality relationship between I and q (slope ~q-1) in the low-q region for all gels – a typical finding for molecules exhibiting long-rod geometry [334]. The low-r skew of the pair distribution functions P(r), shown in (**Figure 5.9-B**), was also consistent with dominant long-rod geometry [334] and r values at peak locations were in line with fibre radius obtained from the TEM micrographs. Notably, P(r) distributions for the co-assembled Fmoc-DDIKVAVK/Fmoc-DIKVAVD system and Fmoc-DDIKVAVL had greater variance than that of Fmoc-DIKVAVD. This feature is suggestive of sary non-rod arrangements as may arise from subtle changes in internal cohesion, leading to increased branching, bundling, flexing or other forms of hierarchical aggregation, consistent with the TEM observations. These results confirm that the superstructures observed under dried, negatively stained TEM were broadly consistent with their hydrated morphology in PBS.

In addition, the hydrated SAP systems were hydrophilic, with all four systems possessing water contact angles below >15° (**Figure 5.10**). The water content of all the hydrogels was 98% as the final concentration was adjusted to 15 mg/mL corresponding to a fixed volume (666.6 ul) for all. Given a starting mass of 10 mg for the peptides, the straightforward calculation resulted in a similar water content for all the SAP.

Rheological experiments were also used to approximate the mesh size of the SAP systems (**Figure 5.11**). Please refer to a thorough introduction and discussion about the rheological evaluation of mesh sizes presented in **Chapter 4, Section 4.7.**

Aimed to engineer hydrogels able to control and provide sustained delivery, we then decided to select four peptide sequences among all libraries to be tested for mesh sizes. We selected

Fmoc-DDIKVAVK already improved for its positive -NH2 groups; DIKVAVD for its negative -COOH groups, DDIKVAVL for its hydrophobic contribution and the co-assembled DDIKVAVK-DIKVAVD because we hypothesized it could result in a consistent positive and negative charges distribution.

The SAP systems possess a shear-thinning behaviour whereby the viscosity of the gels decreases under applied force, enabling the gels to be injectable. To determine, the shear-thinning behaviour of the SAP systems was demonstrated through a series of oscillatory rheological experiments (**Figure 5.12**).

Finally, the biocompatibility of the SAP hydrogels was tested using a CellTiter-Blue cell viability assay. Viability was found to be similar for cells exposed to the different SAP systems and the control sample without any hydrogel (**Figure 5.13**).

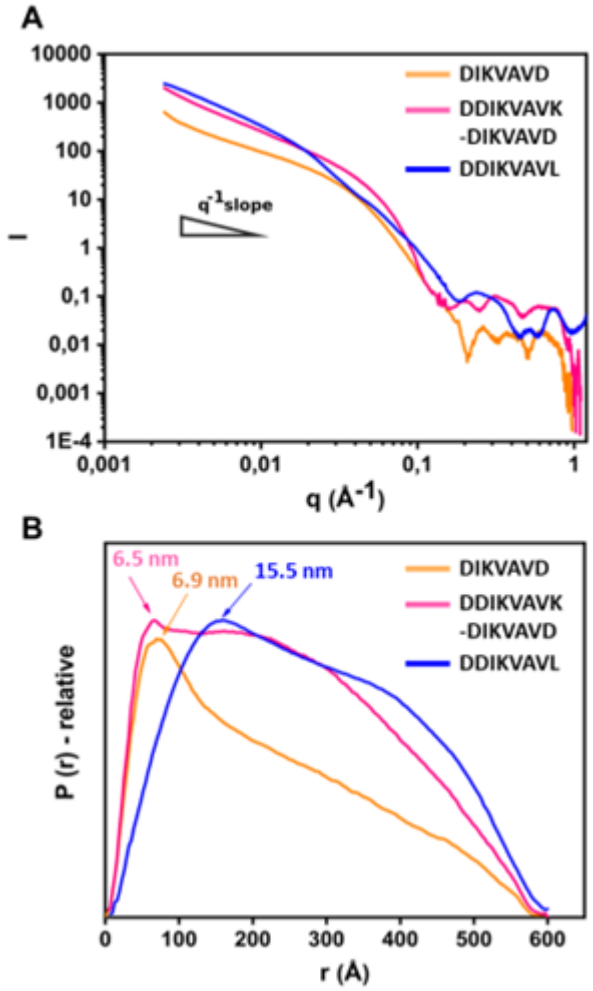


***Figure 5-9 SAXS characterisation results (A and B). (A)*** *Porod plot of scatter intensity vs scattering vector I(q) for three hydrogel carriers. The q-1 slope in the low-q region, which is indicative of long-rod macromolecular arrangements.* ***(B)*** *Associated pair distance distribution functions P(r) with highlighted peak locations. Numbers represent estimates of rod diameter.*

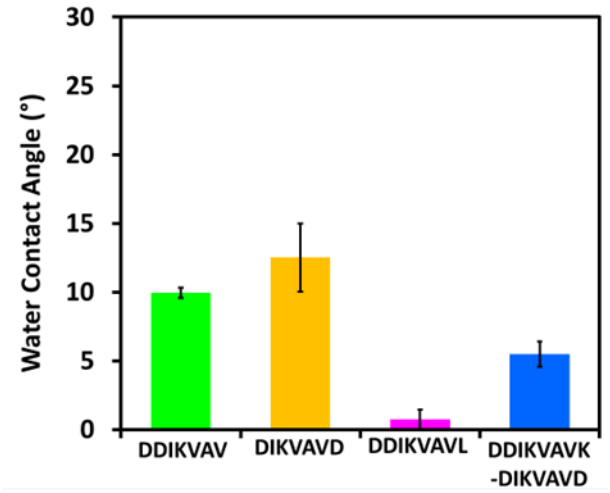


***Figure 5-10 Water contact angles*** *of the SAP hydrogels.*

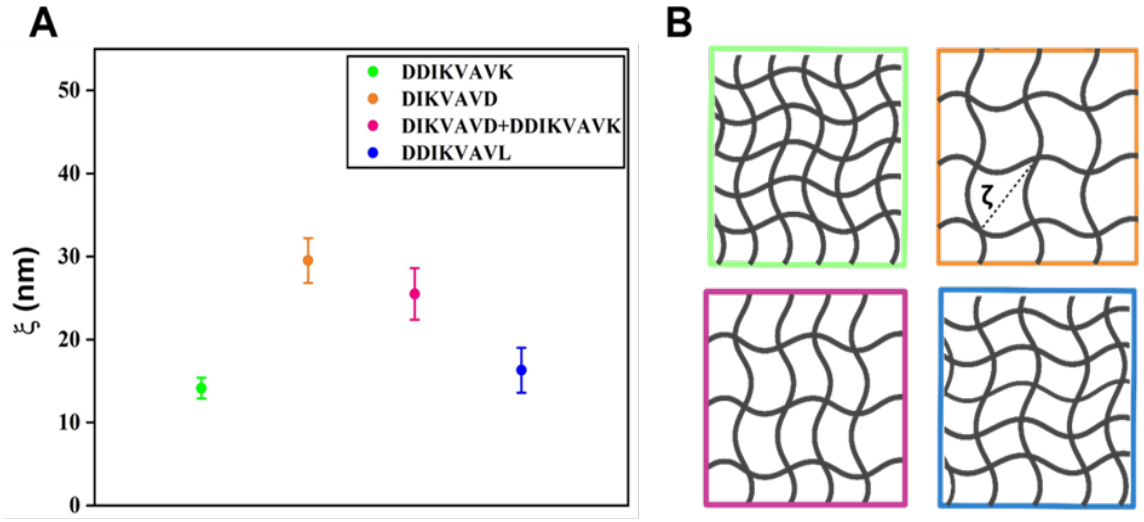


***Figure 5-11 Mesh size (ξ) (A)*** *of the hydrogels. Results showing calculated mesh size values of the hydrogels library following the equation of the theory of rubber elasticity. Schematic of the different mesh sizes* ***(B).***

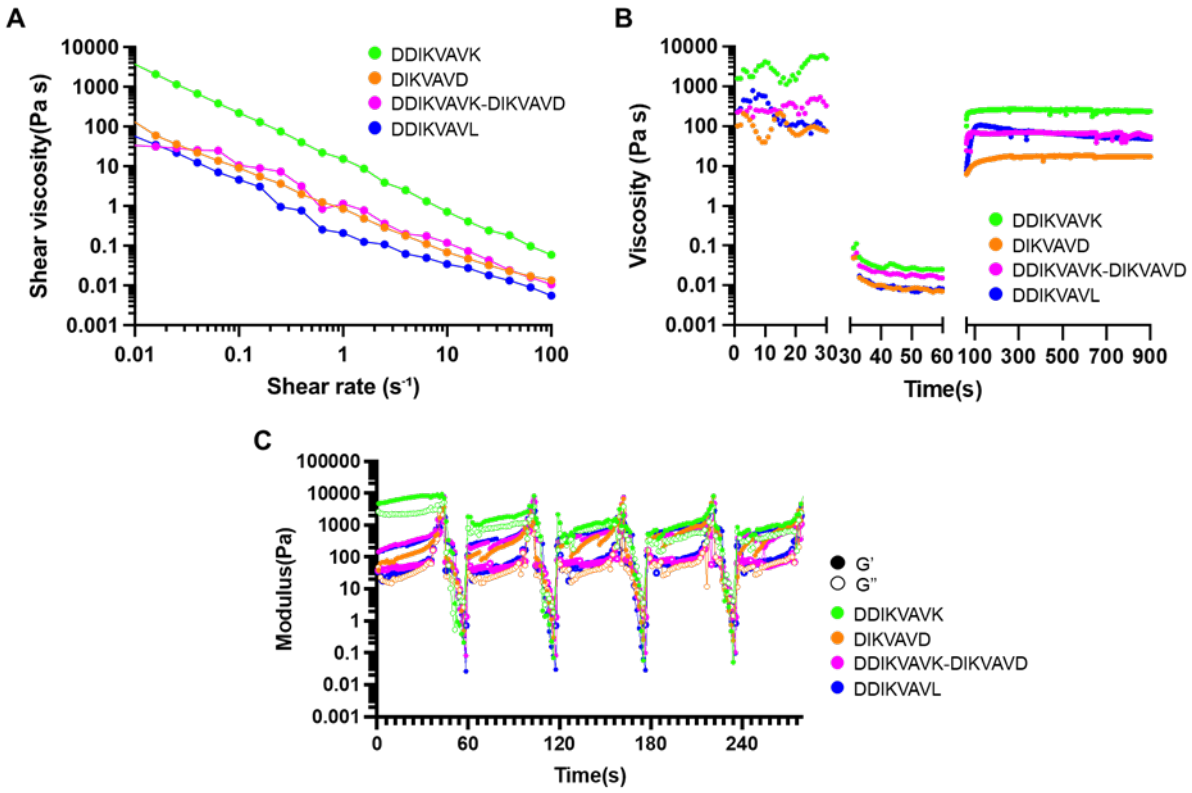


***Figure 5-12 (A)*** *Changes of shear viscosity with increased shear rate, demonstrating the shear-thinning behaviour of the hydrogels.* ***(B)*** *Recovery kinetics of the SAP hydrogels. This was achieved by applying a shear rate at 0.01 s-1 for 30 s, then applying a shear rate at 100 s-1 for 30 s, before finally applying shear rate at 0.01 s-1 for 15 min. This data characterizes the recovery of the shear thinning hydrogels upon removal of shear.* ***(C)*** *An oscillatory rheological experiment investigating changes in modulus overtime. This demonstrates the shear-thinning behaviour of the hydrogels.*

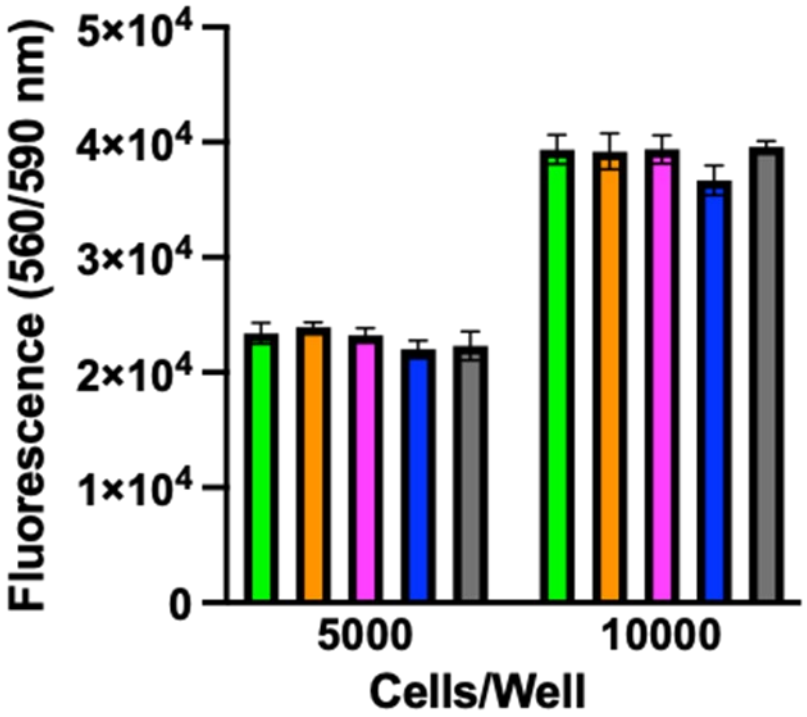


***Figure 5-13 Fluorescence was captured for SH-SY5Y neuroblastoma cells at a cell density of 5 × $10^4$ cells/mL and $10^5$ cells/mL.*** *Cells were prepared at 100 µl/well in a 96-well plate and cultured at 37 °C. CellTiter-Blue® Reagent (20 µl/well) was added and cells were incubated for 3 h before recording fluorescence ($560_{Ex}$/$590_{Em}$) (Fmoc-DDIKVAVK green, Fmoc-DIKVAVD orange, Fmoc-DDIKVAVK-DIKVAVD magenta, Fmoc-DDIKVAVL blue and cells without hydrogels grey).*

### *5.4.4 Vectors Release Profiles Analysis*

The release profiles of the rAAV variants were assessed by quantitative Real-Time PCR (qPCR) (**Figure 5.14**). Homogenous dispersion of vector particles within the materials for all the hydrogels was obtained by thorough mixing of rAAVs during gelation. Fmoc-DDIKVAVL displayed an accelerating release for both rAAV5 and rAAV-DJ, whereas for rAAV2 a consistent linear release profile was observed, demonstrating a constant release rate over 3 days. Fmoc-DIKVAVD also exhibited accelerating release for rAAV5 albeit with a reduction after 48 h. Both Fmoc-DIKVAVD and the co-assembled system showed a burst release for all three serotypes after 24 h, suggesting a repulsive mechanism between these materials and

vector capsids, although Fmoc-DDIKVAVK presented a similar burst release profile for rAAV5.

The release profile analysis revealed various kinetics among which the Higuchi time-lag model appeared to fit most samples tested (seven out of twelve). This model describes the AAVs released from the matrix system (SAPs in this case) driven by Fickian diffusion in which the particles move from high to low concentration over time, thus describing a passive diffusion mechanism. This result displays excellent agreement with the release profiles that were best fitted to the Korsemeyer-Peppas model, such as AAV2-DIKVAVD and AAVDJ-DDIKVAVK-DIKVAVD, where the diffusion exponent was defined as $n>0.5$ pointing to a Fickian diffusion mechanism.

Some release profiles were fitted equally to two models describing a 1st order and a Fickian diffusion (determined by Korsmeyer-Peppas) such as AAVDJ-DDIKVAVK and AAVDJ-DDIKVAVK-DIKVAVD, where the first-order diffusion suggests a concentration-dependent release whilst Fickian diffusion would suggest time dependency. AAV2-DDIKVAVK-DIKVAVD and DDIKVAVK were found to fit a zero-order release which suggests a constant release rate where the remaining concentration of the AAV within the SAP would not play a role and instead, their release would be only time-dependent in a linear manner.

These models provide insight into the release kinetics however, limitations must be accounted for. For instance, the Higuchi model assumes that diffusion occurs unidirectional and constant disregarding the dissolution of the delivery system and border effects. In the same context, the number of samples, particularly at early time points, might incline the fitting towards a particular model. Nevertheless, from the evaluation, it is possible to determine that all the SAP are able to release AAVs and their release is governed, mainly, by diffusion-driven mechanisms. The release rate at which each AAV is released is an interplay between the

material properties from the delivery system (SAP), the intramolecular ionic interaction (such as repulsive charges between negatively charged AAV-SAP) and the determined diffusion mechanism. Correlation values as well as diffusional exponent data are shown in (**Figure 5.15**). Also, cumulative release profile (%) values as well as analysis data from the proportionality constant (K) and the correlation coefficient can be found in (**Figure 5.16**) and (**Table 5-1**) respectively.

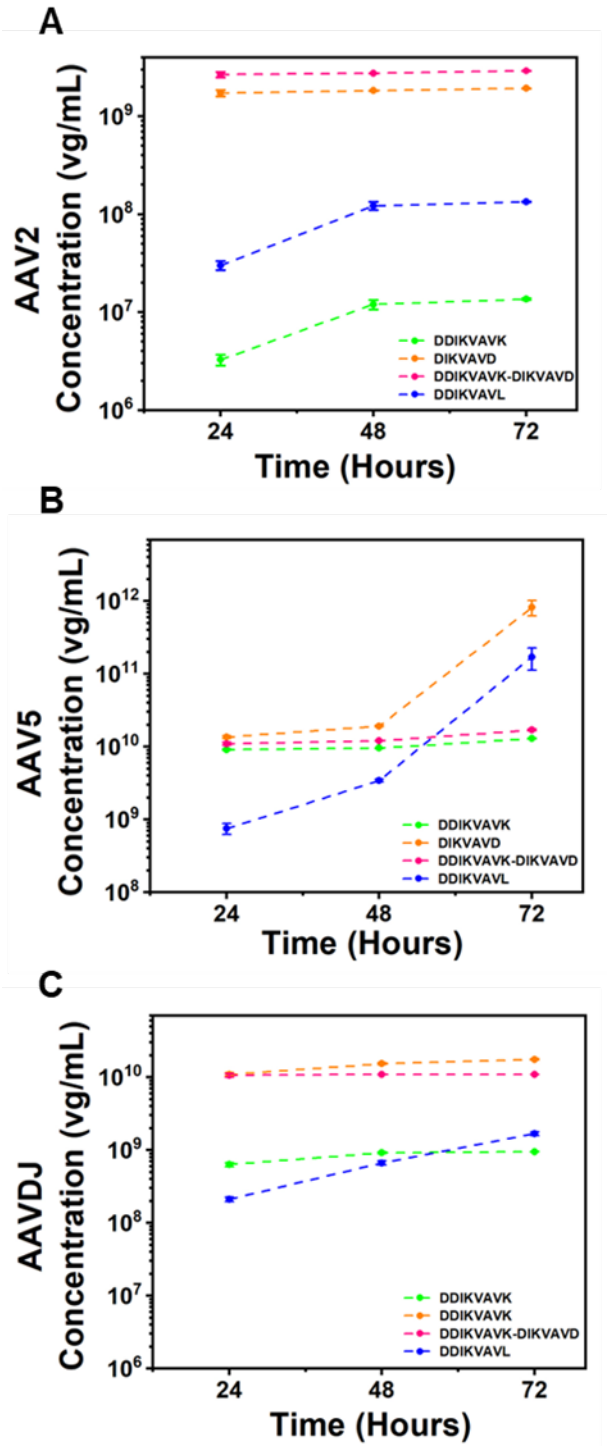


***Figure 5-14 Release profiles of viral vectors from Fmoc-SAP hydrogels.*** *rAAV release profiles for* ***(A)*** *AAV2,* ***(B)*** *AAV5 and* ***(C)*** *AAVDJ were determined by qPCR of vector-encoded DNA. Data represents mean + SD, n=4/rAAV variant/timepoint.*

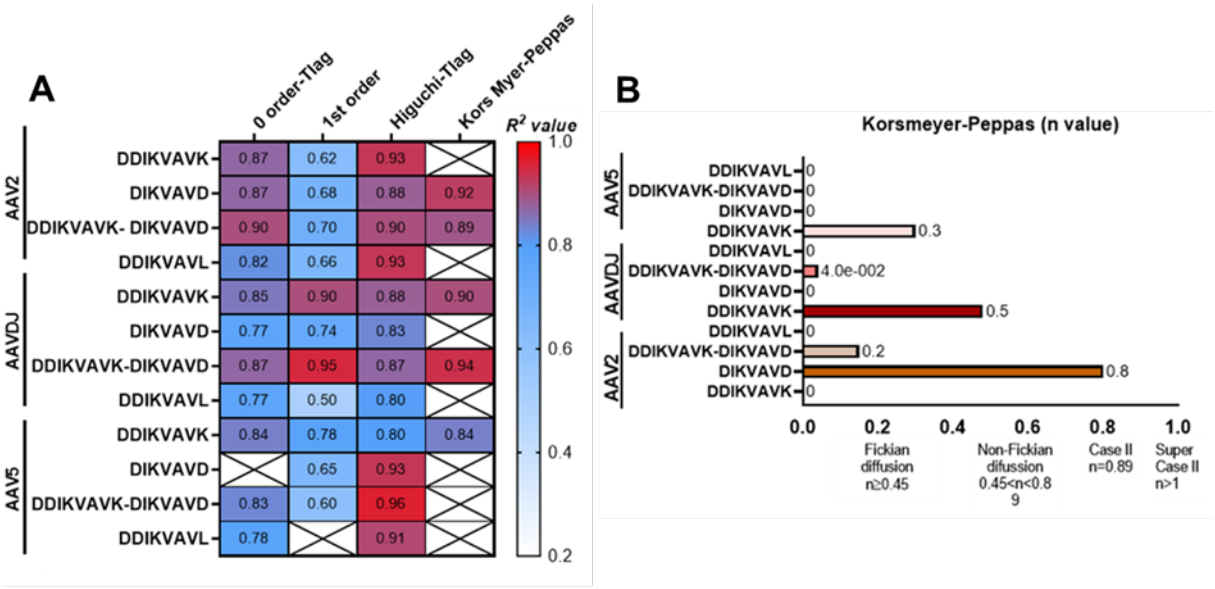


C

| Data/ Model fitting ($R^2$<0.6) | | Model fitting (Max. $R^2$) | Analysis |
|---|---|---|---|
| AAV2 | DDIKVAVK | Higuchi time-lag | Fickian diffusion |
| | DIKVAVD | Korsmeyer-Peppas | n>0.5 Fickian diffusion |
| | DDIKVAVK-DIKVAVD | 0-order | Linear diffusion |
| | DDIKVAVL | Higuchi time-lag | Fickian diffusion |
| AAVDJ | DDIKVAVK | 1st-order/ Korsemeyer-Peppas | Concentration dependent diffusion / Fickian based diffusion |
| | DIKVAVD | Higuchi time-lag | Fickian diffusion |
| | DDIKVAVK-DIKVAVD | 1st order/ Korsmeyer-Peppas | n> 0.5 Fickian diffusion |
| | DDIKVAVL | Higuchi time-lag | Fickian diffusion |
| AAV5 | DDIKVAVK | 0-order/ Korsmeyer-Peppas | 0.45<n<0.89 Non-Fickian diffusion |
| | DIKVAVD | Higuchi time-lag | Fickian diffusion |
| | DDIKVAVK-DIKVAVD | Higuchi time-lag | Fickian diffusion |
| | DDIKVAVL | Higuchi time-lag | Fickian diffusion |

***Figure 5-15 (A)*** *Correlation values (R2) obtained from the mathematical model fitting of the release profiles of rAAVs from SAP biomaterials.* ***(B)*** *Diffusional exponent, n, calculated from the Korsmeyer-Peppas model following equation (5) showing the release regimes according to the value of n.* ***(C)*** *Analysis from the proportionality constant (K) and the correlation coefficient (Table 2) showing the model corresponding to the higher correlation coefficient and its interpretation.*

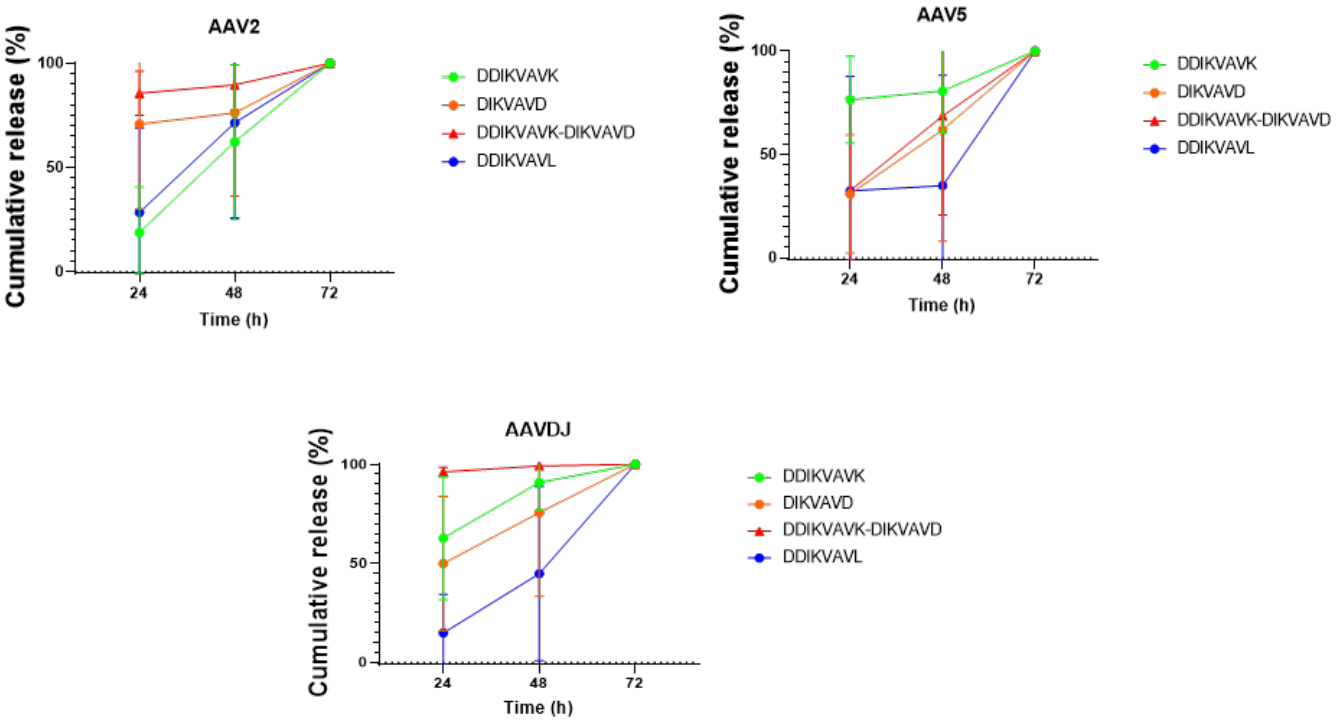


***Figure 5-16 Cumulative release profiles (%) data***

***Table 5-1*** *Analysis from proportionality constant (k) and diffusional coefficient (n).*

| Data/ Model fitting ($R^2$<0.6) | | Zero-order F=k0*t | | Zero-order F = k0*(t-Tlag) | | First order F=100*[1-Exp(-k1*t)] | | Higuchi F=kH*t^0.5 | | Higuchi F=kH*(t-Tlag)^0.5 | | Korsmeyer-Peppas F=kKP*t^n | | |
|---|---|---|---|---|---|---|---|---|---|---|---|---|---|---|
| | | *K* | $R^2$ | *K* | $R^2$ | *K* | $R^2$ | *K* | $R^2$ | *K* | $R^2$ | *K* | *n* | $R^2$ |
| **AAV2** | DDIKVAVK | 1.319 | 0.77 | 1.69 | 0.87 | 0.022 | 0.62 | 9.52 | > | 16 | 0.93 | - | - | - |
| | DIKVAVD | 1.557 | > | 0.61 | 0.87 | 0.093 | 0.68 | 11.96 | > | 9.5 | 0.88 | 53.3 | 0.8 | 0.92 |
| | DDIKVAVK-DIKVAVD | 1.681 | > | 0.3 | 0.9 | 0.086 | 0.7 | 13.16 | > | 6.85 | 0.9 | 57.0 | 0.15 | 0.89 |
| | DDIKVAVL | 1.403 | > | 1.49 | 0.82 | 0.033 | 0.66 | 10.23 | > | 15.4 | 0.93 | - | - | - |
| **AAVDJ** | DDIKVAVK | 1.62 | > | 0.77 | 0.85 | 0.056 | 0.9 | 12.4 | > | 10.5 | 0.88 | 29.85 | 0.48 | 0.9 |
| | DIKVAVD | 1.5 | > | 1.05 | 0.77 | 0.05 | 0.74 | 11.22 | > | 13.8 | 0.83 | - | - | - |
| | DDIKVAVK-DIKVAVD | 1.7 | > | 0.08 | 0.87 | 0.142 | 0.95 | 13.94 | > | 3.82 | 0.87 | 86 | 0.04 | 0.94 |
| | DDIKVAVL | 1.2 | 0.67 | 1.78 | 0.77 | 0.018 | 0.5 | 8.55 | 0.44 | 19.31 | 0.802 | - | - | - |
| **AAV5** | DDIKVAVK | 1.6 | > | 0.49 | 0.84 | 0.084 | 0.78 | 12.37 | > | 7.6 | 0.8 | 44 | 0.3 | 0.84 |
| | DIKVAVD | 1.35 | > | 1.44 | 0.02 | 0.029 | 0.65 | 9.92 | 0.62 | 17.08 | 0.93 | - | - | - |
| | DDIKVAVK-DIKVAVD | 1.39 | > | 1.4 | 0.83 | 0.037 | 0.6 | 10.2 | > | 14.83 | 0.96 | - | - | - |
| | DDIKVAVL | 1.2 | > | 1.4 | 0.78 | 0.052 | > | 8.67 | > | 17.29 | 0.91 | - | - | - |

### *5.4.5 rAAV-DJ Transduction Efficiency Analysis from Fmoc-SAP System*

Next, we evaluated the ability of rAAV-DJ to transduce human astrocytes after release from hydrogel. As expected, the hydrogel provides controlled and sustained release for the embedded rAAV-DJ and the results confirm its transduction efficiency over 72 h (**Figure 5.17**). The post-release transduction efficiency of the rAAV-DJ indicates that the virion remains viable and active when delivered in the SAP system. The percentage of GFP/GFAP was not statistically different across the 3 different time points.

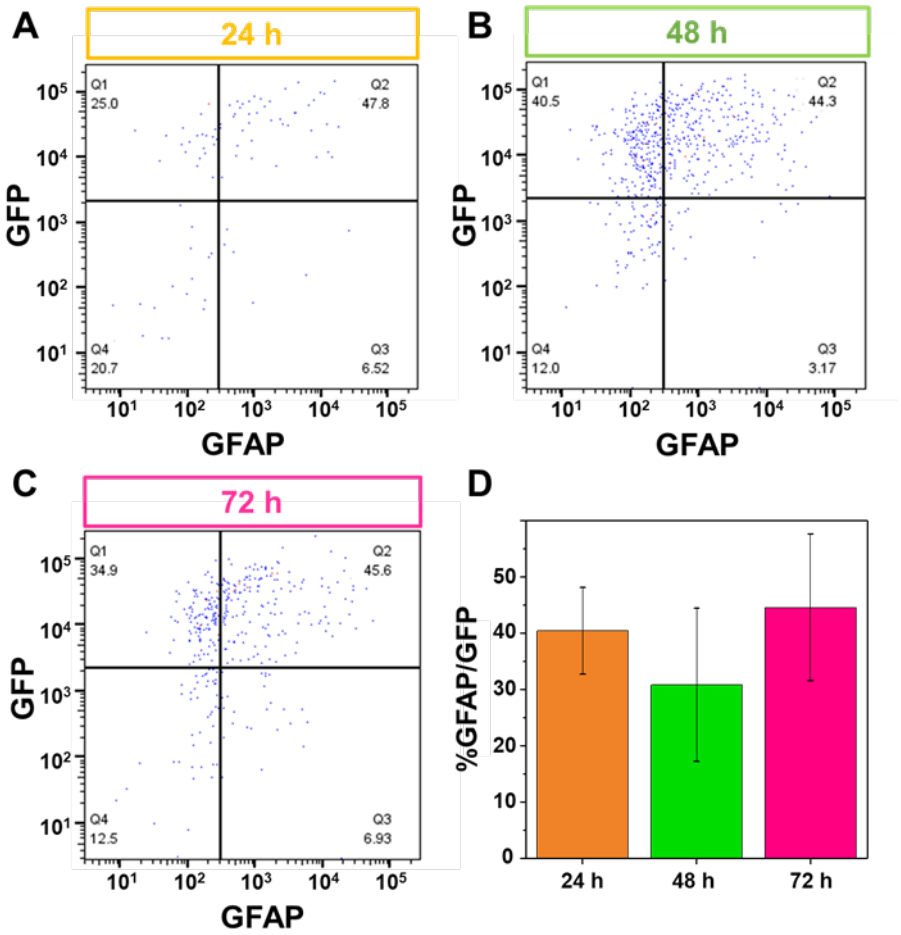


***Figure 5-17 rAAV-DJ Viral vector functionality assessment after release from Fmoc-DIKVAVD on top of the human astrocyte cell line.*** *Percentages of GFP+ GFAP+ cells after* ***(A)*** *24-,* ***(B)*** *48-, and* ***(C)*** *72-hs' release.* ***(D)*** *Quantification of transduced human cell line as represented by percentage of cells positive for GFP and GFAP markers, data represents mean + SD, n=3/rAAV -DJ/timepoint.*

## 5.5 Discussion

In this study, we report on the capability of rAAV2, rAAV5 and rAAV-DJ to transduce specific neural cell types and their potential for controlled delivery to the CNS via bioactive SAPs. We developed a novel delivery material to control the delivery of several AAV variants. Our rationally designed SAP hydrogels were advantageous as they were shown to be well-tolerated *in vivo* while giving us full synthetic control over their delivery properties. These vectors

present diverse physicochemical properties due to their protein capsid composition, which affects not only cell and tissue tropism but also how biomaterial systems should best be tailored to provide desirable controlled release profiles [335].

Importantly, the strength of interactions between the biomaterial and the vectors is crucial in developing longer time courses and specific release profiles, which is essential in tailoring delivery for different therapies depending on the nature of the disease. Specifically, some therapies may benefit from long-term viral vector gene transfer, while others may require short-term or even regulated virus delivery. Similarly, some treatments may demand widespread gene transfer, while for others, localized gene transfer is required. For example, by enhancing the electrostatic interactions available for binding, focal gene delivery could be permitted by restricting the activity of viral vectors to the site of injury. This method holds great potential for targeted and sustained delivery of growth factors in reinnervating damaged tissues such as post-traumatic brain injury or stroke. However, in the case of progressive neurodegenerative disorders such as Parkinson's disease (PD) [336, 337] or Amyotrophic Lateral Sclerosis (ALS) [338, 339], sustained systemic delivery of proteins that promote neuroprotection is more beneficial. Thus, it is important to understand how to develop and improve these vector delivery systems to better treat degeneration or diseases.

The release of an encapsulated payload from a material is, in general, extremely dependent on steric hindrance arising from the mesh size of the hydrogels and the size of the cargo. AAV particles are extremely small with a capsid radius of 25-29 nm [340], which means the vectors show a simple diffusive release profile and are difficult to sufficiently immobilize within any material that has sufficient porosity to enable cellular motility. Therefore, via our facile approach of adjusting SAP sequence to promote non-specific surface interactions, we were able to tailor and improve immobilisation and release using controlled material characteristics, such as increasing the number of charged side chains and the hierarchical bundling of the 1D

nanostructures. Though not shown here, it is anticipated that a higher concentration of peptide in the SAP gel can result in higher crosslinking density. The subsequent smaller mesh size can result in delayed release of AAV from the hydrogel. The lower and slower release of AAVs is expected to have higher transduction efficiency [341]. The stiffness of Fmoc-DDIKVAVK and Fmoc-DDIKVAVL is likely a consequence of the increased contribution of electrostatic interactions; positive lysine groups are available to attract more ions from the solution and generate an increase in the points of association, subsequently reinforcing the interpenetrating network or, similarly, the elevated presence of leucine groups inducing hydrophobic points of entanglement enabling more rigid fibre connections. Overall, Fmoc-DDIKVAVK was able to immobilise viral vectors within its network for all three types of capsid tested, demonstrating an ability to rationally design peptide-based hydrogels for vector immobilization, enabling more controllable delivery of the vectors and possible gene therapy payloads enclosed within them. This was achieved by incorporating stronger attractive forces to increase retention and steric hindrance. rAAV-DJ showed a high tropism for neurons and astrocytes both *in vitro* and *in vivo.* We found that all rAAVs tested could effectively transduce neurons and astrocytes; however, of the three AAV variants tested, only rAAV-DJ demonstrated strong and consistent transduction of both neurons and astrocytes.

## 5.6 Conclusion

We demonstrate that these novel SAPs, in combination with relevant rAAV serotypes, present researchers with the ability to achieve tailored and distinct release profiles within a material that is synergistically optimised for novel therapies in the CNS. This key finding is of high importance for this emerging technology, because thus far there is little knowledge about AAV astrocytic tropism [117, 342, 343]. We demonstrate, for the first time, similar relative tropism for both neurons and astrocytes to that of rAAV-DJ. We suggest, therefore, that rAAV-DJ can be used as a new tool for manipulating the gene expression of both neuronal and astrocytic

cells for many applications. Moreover, we showed that we could control and program the delivery kinetics of the bioengineered rAAV-DJ via rationally designing vector interactions with a tissue- and Context-Specific hydrogel biomaterial. Here, we demonstrated a robust methodology to non-covalently tune the bulk properties of SAP systems whilst retaining a conserved assembly motif that defines the biologically important nanostructure of the scaffolds. As a result, these SAP systems—and the versatility and inherent biocompatibility that they provide—offer significant promise to advance gene therapy towards controllable systems that can help tackle diseases affecting CNS tissue.